Letter

Large-Scale All-Dielectric Metamaterial Perfect Reflectors

Parikshit Moitra,[†] Brian A. Slovick,[‡] Wei li,[§] Ivan I. Kravchencko,[∥] Dayrl P. Briggs,[∥] S. Krishnamurthy,[‡] and Jason Valentine*,[§]

[†]Interdisciplinary Materials Science Program and [§]Department of Mechanical Engineering, Vanderbilt University, Nashville, Tennessee 37212, United States

[‡]Applied Optics Laboratory, SRI International, Menlo Park, California 94025, United States

[∥]Center for Nanophase Materials Sciences, Oak Ridge National Laboratory, Oak Ridge, Tennessee 37831, United States

ABSTRACT: All-dielectric metamaterials offer a potential low-loss alternative to plasmonic metamaterials at optical frequencies. Here, we take advantage of the low absorption loss as well as the simple unit cell geometry to demonstrate large-scale (centimeter-sized) all-dielectric metamaterial perfect reflectors made from silicon cylinder resonators. These perfect reflectors, operating in the telecommunications band, were fabricated using self-assembly based nanosphere lithography. In spite of the disorder originating from the self-assembly process, the average reflectance of the metamaterial perfect reflectors is 99.7% at 1530 nm, surpassing the reflectance of metallic mirrors. Moreover, the spectral separation of the electric and magnetic resonances can be chosen to achieve the required reflection bandwidth while maintaining a high tolerance to disorder. The scalability of this design could lead to new avenues of manipulating light for low-loss and large-area photonic applications.

KEYWORDS: all-dielectric metamaterial, perfect reflector, nanosphere lithography, Mie resonance
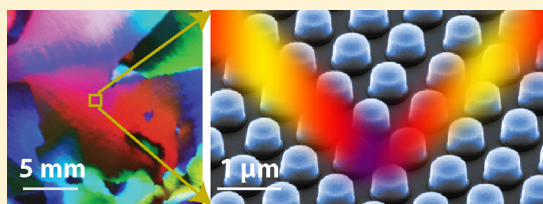
Recently, there has been great interest in finding alternatives to metal-based metamaterials (MMs) in an effort to overcome the free-carrier absorption found in metals at optical frequencies.[1−3] Additionally, metallic unit cells often exhibit complicated geometries that render the optical response anisotropic[3] and necessitate the use of nanoscale lithography techniques, such as electron beam lithography, to pattern the unit cells. These patterning techniques are slow and expensive, prohibiting the designs from being scaled to large areas. Dielectric metamaterials[4−10] based on electric and magnetic Mie resonances[4,6,11−16] in transparent dielectric particles provide a lower-loss alternative to metal-based MMs. Furthermore, due to their simple unit cell geometries such as spheres, cubes, cylinders, and rods,[4,5,16−18] dielectric MMs can potentially be patterned with alternative techniques that allow scaling to large areas.

In recent work, we have demonstrated near-perfect broadband reflection in the telecommunications band using single-negative metamaterials formed from both periodic and disordered lattices of silicon (Si) cylinders.[15,19] Although gold (Au) and silver (Ag) mirrors exhibit high reflection they still absorb ∼2% of light in this band. In place of metallic mirrors, distributed Bragg reflectors (DBRs), made of alternating dielectric layers, are typically used for achieving near-perfect reflection. The primary disadvantage of Bragg reflectors is that the deposition of multiple dielectric materials is a lengthy process which adds to the cost of the product. Realization of perfect reflection from a single-layer large-scale metamaterial, which forms the basis of this article, offers advantages in terms of simple, high-throughput, and low-cost fabrication, and in

turn opens the door to future paint-like coatings of metamaterials for even larger-area implementation.

Additionally, the metamaterial approach provides the freedom to manipulate both the magnetic and electric response of the reflector. Conventional mirrors made from metal and Bragg reflectors operate as electric mirrors in which the reflected electric field undergoes a 180° phase change resulting in an electric field minimum at the mirror surface. Dielectric metamaterial perfect reflectors can exhibit perfect reflection due to both electric and magnetic dipole Mie resonances.[8,15,19,20] In this case, the phase of the reflected electric field can be swept from 180° to 0° by moving from the electric to the magnetic resonance.[20,21] Most importantly, at the magnetic resonance a reflection phase shift of 0° results in an electric field maximum at the surface of the material, strongly enhancing the light−matter interaction[22] of materials placed on the mirror. This field enhancement could be useful for applications, such as surface-enhanced Raman spectroscopy or SERS.

In our previous work,[15] electron beam lithography was used for a proof-of-concept demonstration of a dielectric metamaterial reflector with a sample size of 100 μm × 100 μm. However, for large-area applications, electron beam lithography is impractical. Here, we describe the design and fabrication of large-scale (centimeter-sized) MM perfect reflectors based on silicon (Si) cylinder resonators. Silicon is used as the resonator element due to its transparency and large permittivity at infrared frequencies, as well as its well-developed top-down nanofabrication

processes. Cylindrical resonators are used because they allow spectral separation of the electric and magnetic Mie resonances by changing the aspect ratio (AR) and can be patterned by nanosphere lithography and reactive ion etching (RIE). Using this platform, we demonstrate near-perfect reflection over large centimeter-sized areas with around half a billion resonators comprising the metamaterial. In addition, by studying the effect of lattice disorder originating from the self-assembly patterning process, it was found that the reflectance due to the magnetic resonance is more tolerant to disorder than the electric resonance due to better confinement of the optical mode. This research could lead to the use of large-scale perfect reflectors within the telecommunication band for large-area applications.

The conditions needed to achieve perfect reflection using a thin slab of material are described in the literature.[19] The first condition is complete impedance mismatch with air, namely, the real part of the impedance must be zero. This condition is achieved when $\varepsilon'/\mu' < 0$ (single-negative MM) and $\varepsilon''\mu' = \varepsilon'\mu''$, where the complex permittivity and permeability are given by $\varepsilon' + i\varepsilon''$ and $\mu' + i\mu''$, respectively. The single-negative condition can be satisfied at electric or magnetic resonances, provided that the resonances are spectrally separated. The equation $\varepsilon''\mu' = \varepsilon'\mu''$ is more restrictive but is conveniently satisfied by lossless materials. The second condition for perfect reflection is that the imaginary part of the index (n'') needs to be large to prohibit any evanescent tunneling of light through the slab.

One way to achieve the conditions for perfect reflection is to use electric and magnetic dipole resonances of Si cylinder resonators. In particular, here we arrange the resonators in a hexagonal lattice (Figure 1a) to realize a single-negative metamaterial. S-parameter retrieval[23−25] was performed to extract effective metamaterial properties using the complex transmission and reflection coefficients, which were numerically calculated using full-wave simulations (CST Microwave Studio). Figure 1b illustrates the properties of the metamaterial, namely a region where $\varepsilon' < 0$ and $\mu' > 0$ (electric dipole resonance) at a normalized wavelength ($\lambda_n = \lambda/P$, where P is the lattice period) of 1.34 and $\mu' < 0$ and $\varepsilon' > 0$ (magnetic dipole resonance) at a normalized wavelength of 1.65. Figure 1c shows the metamaterial reflection spectra, demonstrating perfect reflection at these two wavelengths. The inset shows the corresponding electric and magnetic field plots, illustrating that the two reflection peaks correspond to electric and magnetic dipole resonances.

In order to fabricate the metamaterial on a large scale, we utilized a modified version of nanosphere lithography. First, polystyrene (PS) spheres (820 nm in diameter) were self-assembled into a monolayer hexagonal close packed lattice at an air−water interface[26−29] (Figure 2a). Then, two key techniques, orientating the PS spheres and maximizing their concentration, were used to expedite the formation of a wafer-scale close-packed pattern with millimeter scale single grain sizes. The reorientation of PS particles at the air−water interface was accelerated by perturbing the particles with a gentle and controlled flow (5 L/min) of compressed air through a flat nozzle.[26] We maximized the concentration of PS particles at the air−water interface by minimizing loss of PS particles in the liquid phase[30] (see Methods for details). After formation of the close-packed monolayer of PS particles at the air−water interface, the pattern was transferred onto an silicon-on-insulator (SOI) substrate (SOITEC) placed below the water
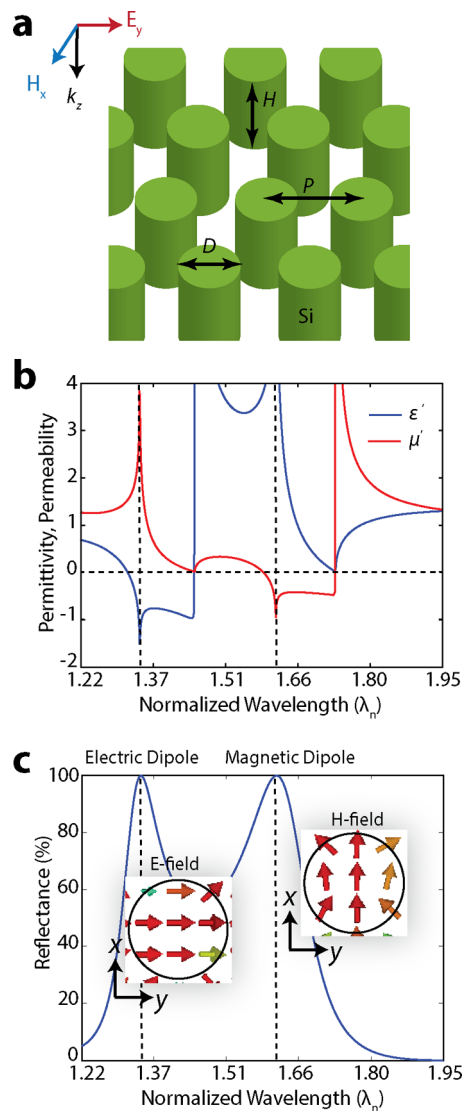

Figure 1. (a) Schematic of the metamaterial formed from a hexagonal lattice of Si cylinder unit cells with height H and diameter D. The periodicity of the lattice is P. (b) Extracted real parts of the effective permittivity (ε') and permeability (μ') of the metamaterial with respect to normalized wavelength $\lambda_n = \lambda/P$. The diameter and height, normalized to P, are $D_n = 0.39$ and $H_n = 0.49$, respectively. Dashed lines indicate the positions of resonances. (c) Reflectance plot with respect to the normalized wavelength demonstrating perfect reflectance at both the electric and magnetic dipole resonances. In the inset the electric and magnetic field vector plots confirm the presence of electric and magnetic dipolar resonances in the cylinders.

surface at a 10° inclination angle[31] by slowly draining the water from the Teflon bath. An image of a PS pattern assembled on an SOI substrate (2 cm × 2 cm) is shown in Figure 2b. The strong opalescence indicates the formation of a close-packed pattern with individual single grain sizes varying from 2 mm to 10 mm. These individual grains correspond to single crystals comprised of hexagonal close-packed lattices of PS particles oriented in a particular direction. These single crystals nucleate at different spatial positions before coming together to form a polycrystalline layer during the assembly process. Next, the PS spheres (SEM image in Figure 2c) were downscaled in size to 560 nm (Figure 2d) using an isotropic oxygen plasma etch. This pattern served as an etch mask for the subsequent RIE processing of Si using SF_6/C_4F_8 chemistry. Figure 2e,f show SEM images of the
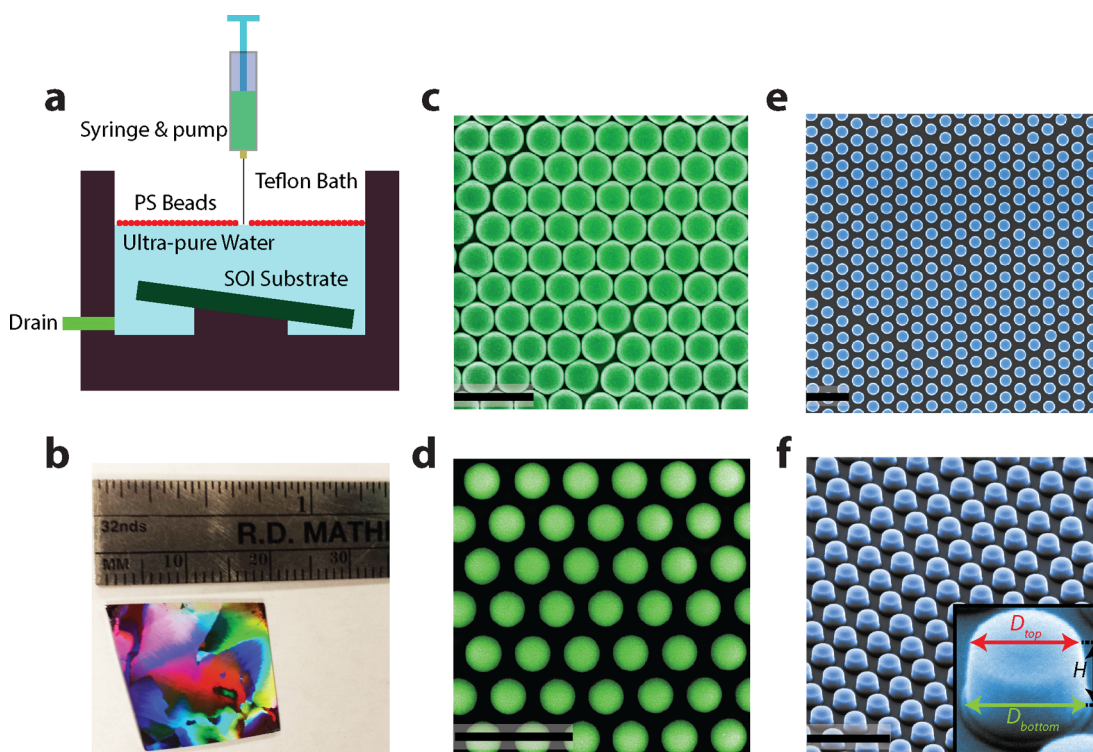
Figure 2. (a) Schematic of the self-assembly based nanosphere lithography technique. PS particles are first assembled in a monolayer at an air–water interface. The monolayer is then transferred to the SOI substrate by slowly draining the water from the bottom of the Teflon bath. (b) Camera image of the large-scale pattern (∼2 cm × 2 cm) of close-packed polystyrene spheres on an SOI substrate. Strong opalescence suggests fabrication of a close packed pattern. The pattern also exhibits formation of large single grains (mm size). (c–f) SEM images of (c) hexagonal close-packed polystyrene spheres (green, false color) of diameter 820 nm and (d) polystyrene spheres downscaled in size to 560 nm using isotropic O_2 plasma etching. (e) Top view of the final metamaterial structure consisting of an array of Si cylinders (blue, false color). The cylinders were formed by using SF_6/C_4F_8 reactive ion etch chemistry. (f) Tilted view (45°) of the final metamaterial consisting of an array of Si cylinders (blue, false color). The inset shows an SEM image of a single Si resonator with a top diameter (D_{top}), bottom diameter (D_{bottom}) and height (H) of 480, 554, and 335 nm, respectively. The scale bar for the SEM images (c–f) is 2 μm.

top and isometric views of the final metamaterial (after removal of PS mask) consisting of Si cylinders (D_{top} = 480 nm, D_{bottom} = 554 nm, H = 335 nm, and P = 820 nm) arranged in a hexagonal lattice. The SEM images along with the optical image clearly demonstrate that nanosphere lithography can yield high quality dielectric resonators over a large area.

The size variations in PS spheres (coefficient of variance (CV) ≤ 3%) and the self-assembly process resulted in some disorder in the metamaterial. The resonator positional disorder (4.1%) was calculated by first finding the standard deviation of nearest neighbor distances for 188 resonator samples (SEM image) and then normalizing the standard deviation to the ideal periodicity (820 nm). To characterize the role of disorder, the reflectance from the metamaterial was measured using a custom-built infrared (IR) microscope with white light illumination at normal incidence to the metamaterial surface and was compared with the simulated reflectance from a perfectly periodic metamaterial (Figure 3a). The simulated reflectance was calculated using the dispersive optical properties of Si measured by ellipsometry. To properly compare with the measured spectra, the simulations include a 2 μm SiO_2 layer below the Si resonators and a semi-infinite Si substrate. The reflectance from the metamaterial reflector was first normalized to the reflectance from a silver mirror. The absolute reflectance of the silver mirror was also measured and used to calculate the absolute reflectance of the metamaterial reflector. The maximum reflectance measured at normal incidence was 99.7%

at 1530 nm, which is in excellent agreement with the simulation. It is important to note that the maximum reflectance from the metamaterial reflector surpasses the average reflectance of the silver mirror (measured as 97.7%) and a gold mirror (99%)[32] in the telecommunications wavelength band.

To characterize the uniformity of the reflectance over a large area, we carried out a spatial scanning of reflectance at 1530 nm over a 10 mm-by-10 mm area of the fabricated sample. The spatial reflectance scan, shown in Figure 3b, indicates an average reflectance of 99.2% with a standard deviation over the entire area of only 0.21%, which is at the same level as the measurement noise of 0.25%. The uniformity of the peak reflectance over such large areas indicates that the homogenized properties of the metamaterial hold over large areas despite the disorder of the lattice.

To illustrate the angle-resolved behavior of the perfect reflector we have plotted the theoretical and experimental reflectance at 1530 nm as a function of the angle of incidence for s- (electric field parallel to the surface) and p-polarizations (magnetic field parallel to the surface) in Figure 4a. In the experimental measurements, the sample was mounted in an integrating sphere and reflectance was measured for incident angles ranging from 10° to 45° with respect to the normal direction of the substrate. The theoretical and experimental data are in good agreement and it can be observed that the reflectance for both polarizations is relatively constant up to an angle of 15°. For larger angles, the reflectance for s-polarized
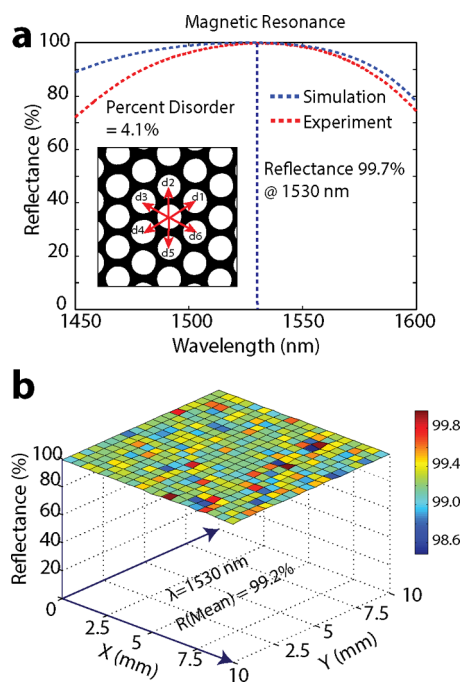
Figure 3. (a) Measured and simulated reflectance of the metamaterial demonstrated in Figure 2. A maximum reflectance of 99.7% is achieved at 1530 nm. In the inset a binarized SEM image is shown. The percent disorder calculated using 188 resonator samples is 4.1%. d1 through d6 denote the six nearest neighbor distances from a particular resonator. The simulated reflectance was calculated using a perfectly periodic metamaterial. (b) Spatial scan of reflectance at 1530 nm over a 10 mm by 10 mm area of the metamaterial. The average reflectance over the entire area is 99.2% with measurement error of ±0.25%.

light remains relatively constant while the *p*-polarization experiences a marked decrease in reflectivity. The difference in the simulated and measured reflectance at higher angles of incidence is attributed to the fact that disorder in lattice was not considered in simulation but influences the measured reflectance. Higher angles of incidence lead to a larger phase shift between the resonators amplifying perturbations in their resonance frequency. We also find that the higher-order diffraction at 1530 nm are negligible for all angles of incidence, indicating that the most of the incident energy is reflected into the zeroth order specular mode. To demonstrate the uniformity of its specular reflectance, a Vanderbilt University logo was reflected off the metamaterial at a 20° incident angle and imaged using an IR camera at 1530 nm. The diameter of the logo on the MM reflector surface was approximately 7 mm. The image produced by the MM reflector is compared to that produced by a metallic mirror in Figure 4b. No distortion in the image was found in the case of MM reflector compared to the case of the planar metallic mirror.

To better understand the polarization and angular dependence of the reflection, the numerically calculated reflectance spectra for *s*- and *p*-polarizations are plotted as a function of incident angle in Figure 4c and e, respectively. For *s*-polarization the magnetic dipole mode[15,33,34] maintains a relatively constant spectral position with increasing angle of incidence, as demonstrated in the reflectance spectrum in Figure 4c. The presence of the magnetic dipole at an 80° incident angle and illumination wavelength of 1530 nm is further supported by the field plot in Figure 4d. However, for *p*-polarization, increasing the illumination angle results in a red-shift of the magnetic mode (Figure 4e), decreasing reflection at 1530 nm.
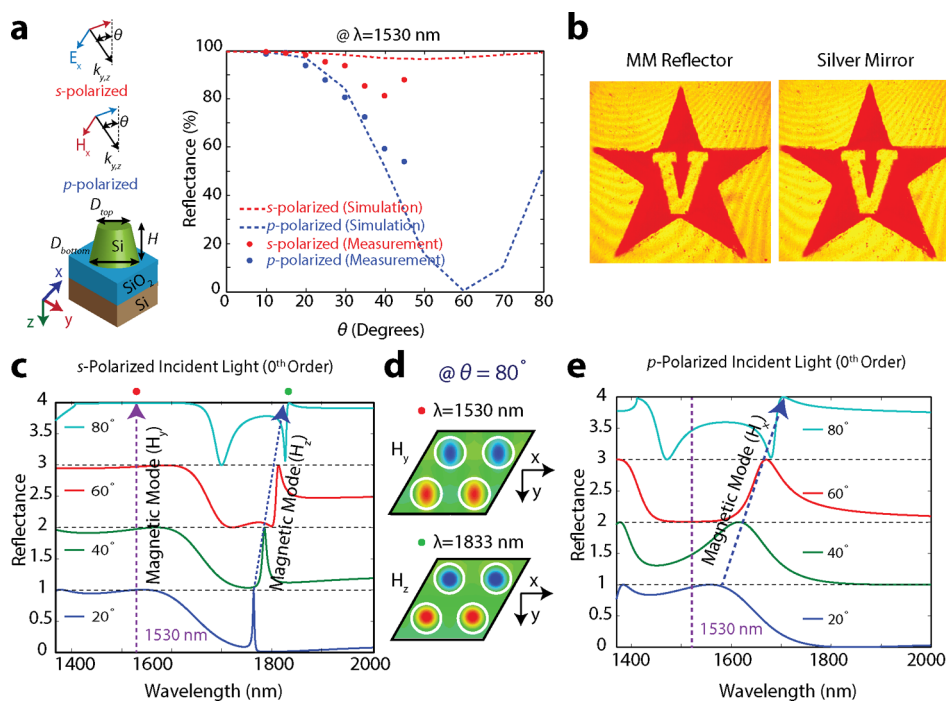

Figure 4. (a) Schematic of *s*- and *p*-polarized incident light and the simulated and experimentally measured angle-resolved reflectances at 1530 nm. Reflectance was measured for incident angles between 10° and 45°. (b) IR camera images of a Vanderbilt logo that was reflected off of the MM reflector and a silver mirror with a 20 degree angle of incidence. The MM reflector leads to strong specular reflectance. The beam diameter at the surfaces of the reflectors was ~7 mm. (c) Simulated angle-resolved specular reflectance for *s*-polarized light at 20, 40, 60, and 80° angle of incidence. (d) Magnetic field plots (H_y and H_z) illustrating magnetic dipole resonances. (e) Simulated angle-resolved specular reflectance for *p*-polarized light at 20, 40, 60, and 80° angle of incidence.

Another interesting feature to note here is the formation of a sharp reflectance peak due to vertical magnetic dipole resonance (H_z). The field plot corresponding to the vertical magnetic dipole at 1833 nm and an 80° angle of incidence is illustrated in Figure 4d.

It is also critical to understand what role disorder plays on the electric and magnetic resonances of the surface. Figure 5a compares the measured reflectance from a MM with
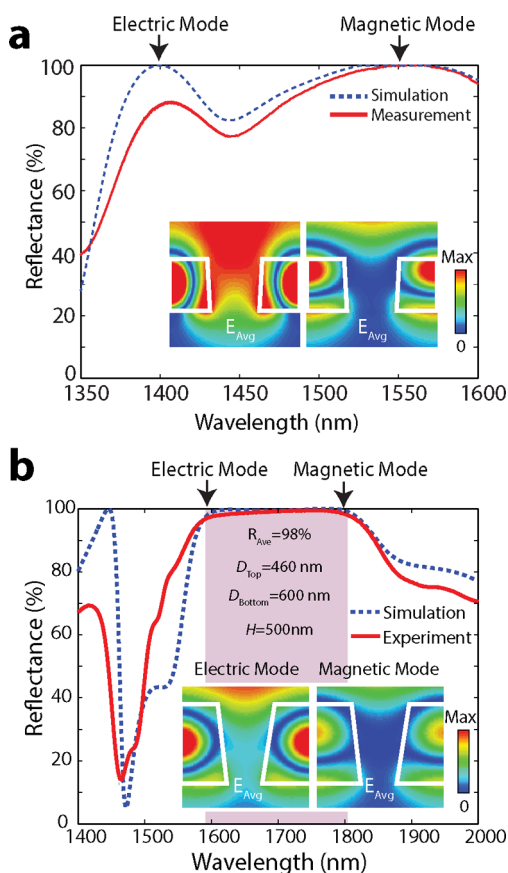

Figure 5. (a) Comparison of the simulated reflectance spectra of a perfectly periodic metamaterial and the measured reflectance spectra of a metamaterial with 4% disorder in the lattice. The figure demonstrates the higher tolerance to disorder of the magnetic mode compared to the electric mode. Simulated time-averaged electric fields are shown for the two modes in the inset. The electric mode results in more field being located outside of the resonator, resulting in a lower tolerance to disorder. (b) Simulated and experimental reflectances of a broadband mirror demonstrating strong reflectance over a 200 nm bandwidth with an average reflectance (experiment) of 98%. The resonator dimensions are D_{top} = 460 nm, D_{bottom} = 600 nm, H = 500 nm and the periodicity of lattice is P = 820 nm. Simulated time-averaged electric field for the electric and magnetic modes are shown in the inset. Better confinement of electric mode is apparent.

a disorder of approximately 4% and the simulated reflectance from a perfectly periodic metamaterial with a hexagonal lattice (P = 820 nm). While the measured reflectance shows excellent agreement with the simulated reflectance at the magnetic resonance, it is approximately 15% less than the simulated reflectance at the electric resonance. This is because the electric mode is leaking into the regions between the resonators, whereas the magnetic mode is well confined within the resonator. To achieve tolerance to disorder, the electric mode must be more confined inside the resonator which can be

achieved by increasing the aspect ratio. In Figure 5b we present the simulated and measured reflectance from a metamaterial with a resonator height of 500 nm, increased from 335 nm in the original design. The new design has a 200 nm broad reflectance band centered at 1700 nm with an average measured reflectance greater than 98%. The simulated electric field plot shows better confinement for the electric mode inside the resonators (D_{top} = 460 nm, D_{bottom} = 600 nm, H = 500 nm, P = 820 nm) than that observed in Figure 5a which ultimately results in higher reflectance near the electric mode in the fabricated samples.

It is interesting to note that the metamaterial perfect reflector design, in contrast with metallic mirrors, can be used to realize magnetic mirrors in which the maxima of the electric field is located at the surface of the metamaterial. However, only when the magnetic mode is spectrally separated from the electric mode will the perfect reflection due to the magnetic mode lead to the formation of a magnetic mirror. Due to the moderate dielectric constant of Si, the resonators must be carefully designed to minimize coupling while at the same time avoiding diffraction. In our approach to design a magnetic mirror with Si cylinder resonators we kept the periodicity (P = 820 nm) and height of the resonators (H = 335 nm) the same as in the original design while increasing the aspect ratio by reducing the diameter. This causes the electric and magnetic modes to become more separated from one another[14,15] while decreasing the coupling between the resonators due to greater physical separation. This can be achieved using a metamaterial design with AR = H/D = 1.675 and D_n = D/P = 0.24. As shown in Figure 6a, the reflection phase at the magnetic-dipole resonance (λ_n = 1.16) remains close to zero, consistent with a magnetic mirror, while the difference in reflection phase between the electric (λ_n = 1.01) and magnetic resonances is close to 180°. Figure 6b illustrates the phase offset[20] of the reflected electric field of the metamaterial reflector compared to a perfect electric conductor (PEC), demonstrating the magnetic mirror response. Furthermore, the metamaterial reflector shows no offset in reflection phase compared to a PEC at the electric resonance, as shown in Figure 6c. It should be noted that due to the decreased normalized wavelength, these magnetic mirrors experience diffraction at incident angles greater than 10°.

In summary, we demonstrated that dielectric MMs can overcome two serious issues of plasmonic metamaterials—absorption loss and scalability limitations. Furthermore, these reflectors are tolerant to disorder and can be designed for either narrowband or broadband performance. To the best of our knowledge, this is the first reported effort for scaling up fabrication of all-dielectric metamaterials to large areas using a simple, low-cost, and high-throughput method. This research could pave the way toward experimental demonstrations of other large-scale metamaterials and metasurfaces, such as Huygens' surfaces,[14,35] that possess more complex optical properties such as overlapped electric and magnetic modes.

■ METHODS

Nanosphere Lithography. Commercially available polystyrene spheres in an aqueous solution (10 wt %) were mixed with an equal volume of ethanol and injected on to the water surface at a rate of 5 μL/min using a syringe pump. A tygon tube with a diameter of 0.5 mm was connected to the syringe and held upright with the bevel tip of the tube just touching the water (18.2 M-Ohm) surface. This results in the formation of a meniscus onto which PS particles are deposited. This technique
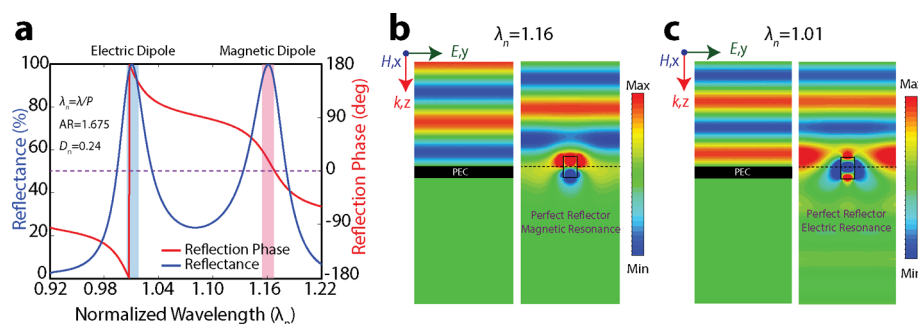
Figure 6. (a) Simulated reflectance with respect to normalized wavelength. Perfect reflection is present for both the spectrally separated electric and magnetic modes. This results in a perfect electric reflector with a reflection phase close to 180°, the same as a metallic mirror. The magnetic mode however has a reflection phase close to zero. (b) Electric field plots demonstrating the phase offset due to a metamaterial perfect magnetic reflector with respect to a perfect electric conductor (PEC). (c) Electric field plots demonstrating no phase offset between a metamaterial perfect electric reflector with respect to a perfect electric conductor (PEC).

reduces the chance of PS particles falling into the liquid phase. Contrary to the common practice of using a surfactant (SDS or Triton-X-100) to facilitate the self-assembly process, here we avoided using any surfactant as PS particles fell into the liquid phase more readily with increasing surfactant concentration. The self-assembly process was facilitated by reorienting the PS particles on the water surface using a controlled flow of compressed air through a flat nozzle (5 L/min) that was aimed at the water surface. This perturbation assisted self-assembly process led to better packing and larger single grains. It took 5−6 min to cover the entire water surface held in a 100 mm diameter cylindrical Teflon bath. The defects in the close-packed monolayer formed at the air−water interface are unavoidable due to size variations in the PS particles, resulting in stress within the pattern. To relieve the stress and to accommodate the defects such as PS particles randomly dispersing in the monolayer, the pattern was transferred on a substrate at a 10° inclination angle. The substrate was placed below the water surface and the film was deposited by slowly draining the water from the bottom of the bath. The overall process of pattern transfer and drying the substrate in air took 20−25 min.

Simulation. All the simulation results, including reflectance plots and field profiles, were calculated using the Frequency Domain (FD) solver of CST Microwave Studio. In all of the simulations, periodic boundaries were employed in the x and y directions. Ports (18 modes calculated) were used on the input and output planes.

■ AUTHOR INFORMATION

Corresponding Author
*E-mail: jason.g.valentine@vanderbilt.edu.

Notes
The authors declare no competing financial interest.

■ ACKNOWLEDGMENTS

■ REFERENCES

(1) Boltasseva, A.; Atwater, H. A. Materials Science. Low-Loss Plasmonic Metamaterials. *Science* **2011**, *331* (6015), 290−291.

(2) Zheludev, N. I. Applied Physics. The Road Ahead for Metamaterials. *Science* **2010**, *328* (5978), 582−583.

(3) Soukoulis, C. M.; Wegener, M. Past Achievements and Future Challenges in the Development of Three-Dimensional Photonic Metamaterials. *Nat. Photonics* **2011**, *5* (9), 523−530.

(4) Vynck, K.; Felbacq, D.; Centeno, E.; Căbuz, A.; Cassagne, D.; Guizal, B. All-Dielectric Rod-Type Metamaterials at Optical Frequencies. *Phys. Rev. Lett.* **2009**, *102* (13), 133901.

(5) Popa, B.-I.; Cummer, S. Compact Dielectric Particles as a Building Block for Low-Loss Magnetic Metamaterials. *Phys. Rev. Lett.* **2008**, *100* (20), 207401.

(6) Zhao, Q.; Zhou, J.; Zhang, F.; Lippens, D. Mie Resonance-Based Dielectric Metamaterials. *Mater. Today* **2009**, *12* (12), 60−69.

(7) Evlyukhin, A. B.; Reinhardt, C.; Seidel, A.; Luk'yanchuk, B. S.; Chichkov, B. N. Optical Response Features of Si-Nanoparticle Arrays. *Phys. Rev. B* **2010**, *82* (4), 045404.

(8) Ginn, J. C.; Brener, I.; Peters, D. W.; Wendt, J. R.; Stevens, J. O.; Hines, P. F.; Basilio, L. I.; Warne, L. K.; Ihlefeld, J. F.; Clem, P. G.; Sinclair, M. B. Realizing Optical Magnetism from Dielectric Metamaterials. *Phys. Rev. Lett.* **2012**, *108* (9), 097402.

(9) Holloway, C. L.; Kuester, E. F.; Baker-Jarvis, J.; Kabos, P. A Double Negative (DNG) Composite Medium Composed of Magneto-dielectric Spherical Particles Embedded in a Matrix. *IEEE Trans. Antennas Propag.* **2003**, *51* (10), 2596−2603.

(10) O'brien, S.; Pendry, J. B. Magnetic Activity at Infrared Frequencies in Structured Metallic Photonic Crystals. *J. Phys.: Condens. Matter* **2002**, *14* (25), 6383−6394.

(11) Bohren, C. F.; Huffman, D. R. *Absorption and Scattering of Light by Small Particles*; John Wiley & Sons: New York, 1983; p 544.

(12) Schuller, J.; Zia, R.; Taubner, T.; Brongersma, M. Dielectric Metamaterials Based on Electric and Magnetic Resonances of Silicon Carbide Particles. *Phys. Rev. Lett.* **2007**, *99* (10), 107401.

(13) Peng, L.; Ran, L.; Chen, H.; Zhang, H.; Kong, J. A.; Grzegorczyk, T. M. Experimental Observation of Left-Handed Behavior in an Array of Standard Dielectric Resonators. *Phys. Rev. Lett.* **2007**, *98*, 157403.

(14) Staude, I.; Miroshnichenko, A. E.; Decker, M.; Fofang, N. T.; Liu, S.; Gonzales, E.; Dominguez, J.; Luk, T. S.; Neshev, D. N.; Brener, I.; Kivshar, Y. Tailoring Directional Scattering through Magnetic and Electric Resonances in Subwavelength Silicon Nanodisks. *ACS Nano* **2013**, *7* (9), 7824−7832.

(15) Moitra, P.; Slovick, B. A.; Gang, Y. Z.; Krishnamurthy, S.; Valentine, J. Experimental Demonstration of a Broadband All-Dielectric Metamaterial Perfect Reflector. *Appl. Phys. Lett.* **2014**, *104* (17), 171102.

(16) Moitra, P.; Yang, Y.; Anderson, Z.; Kravchenko, I. I.; Briggs, D. P.; Valentine, J. Realization of an All-Dielectric Zero-Index Optical Metamaterial. *Nat. Photonics* **2013**, *7* (10), 791−795.

(17) Fu, Y. H.; Kuznetsov, A. I.; Miroshnichenko, A. E.; Yu, Y. F.; Luk'yanchuk, B. Directional Visible Light Scattering by Silicon Nanoparticles. *Nat. Commun.* **2013**, *4*, 1527.

(18) García-Etxarri, A.; Gómez-Medina, R.; Froufe-Pérez, L. S.; López, C.; Chantada, L.; Scheffold, F.; Aizpurua, J.; Nieto-Vesperinas, M.; Sáenz, J. J. Strong Magnetic Response of Submicron Silicon Particles in the Infrared. *Opt. Express* **2011**, *19* (6), 4815−4826.

(19) Slovick, B.; Yu, Z. G.; Berding, M.; Krishnamurthy, S. Perfect Dielectric-Metamaterial Reflector. *Phys. Rev. B* **2013**, *88* (16), 165116.

(20) Liu, S.; Sinclair, M. B.; Mahony, T. S.; Jun, Y. C.; Campione, S.; Ginn, J.; Bender, D. A.; Wendt, J. R.; Ihlefeld, J. F.; Clem, P. G.; Wright, J. B.; Brener, I. Optical Magnetic Mirrors without Metals. *Optica* **2014**, *1* (4), 250.

(21) IEEE Xplore Full-Text HTML: Experimental demonstration of an optical artificial perfect magnetic mirror using dielectric resonators. http://ieeexplore.ieee.org/xpls/icp.jsp?arnumber=6349206 (accessed Feb 10, 2015).

(22) Esfandyarpour, M.; Garnett, E. C.; Cui, Y.; McGehee, M. D.; Brongersma, M. L. Metamaterial Mirrors in Optoelectronic Devices. *Nat. Nanotechnol.* **2014**, *9* (7), 542−547.

(23) Chen, X.; Grzegorczyk, T.; Wu, B.-I.; Pacheco, J.; Kong, J. Robust Method to Retrieve the Constitutive Effective Parameters of Metamaterials. *Phys. Rev. E* **2004**, *70* (1), 016608.

(24) Smith, D. R.; Vier, D. C.; Koschny, T.; Soukoulis, C. M. Electromagnetic Parameter Retrieval from Inhomogeneous Metama-terials. *Phys. Rev. E* **2005**, *71* (3), 036617.

(25) Szabo, Z.; Park, G.-H.; Hedge, R.; Li, E.-P. A Unique Extraction of Metamaterial Parameters Based on Kramers−Kronig Relationship. *IEEE Trans. Microwave Theory Tech.* **2010**, *58* (10), 2646−2653.

(26) Meng, X.; Qiu, D. Gas-Flow-Induced Reorientation to Centimeter-Sized Two-Dimensional Colloidal Single Crystal of Polystyrene Particle. *Langmuir* **2014**, *30* (11), 3019−3023.

(27) Rybczynski, J.; Ebels, U.; Giersig, M. Large-Scale, 2D Arrays of Magnetic Nanoparticles. *Colloids Surf., A* **2003**, *219* (1−3), 1−6.

(28) Ho, C.-C.; Chen, P.-Y.; Lin, K.-H.; Juan, W.-T.; Lee, W.-L. Fabrication of Monolayer of Polymer/Nanospheres Hybrid at a Water−Air Interface. *ACS Appl. Mater. Interfaces* **2011**, *3* (2), 204−208.

(29) Barcelo, S. J.; Lam, S.; Gibson, G. A.; Sheng, X.; Henze, D. Nanosphere Lithography Based Technique for Fabrication of Large Area, Well Ordered Metal Particle Arrays Abstract: Nanosphere Lithography Based Technique for Fabrication of Large Area, Well Ordered Metal Particle Arrays. 2012.

(30) Zhang, J.-T.; Wang, L.; Chao, X.; Velankar, S. S.; Asher, S. a. Vertical Spreading of Two-Dimensional Crystalline Colloidal Arrays. *J. Mater. Chem. C* **2013**, *1* (38), 6099.

(31) Stavroulakis, P. I.; Christou, N.; Bagnall, D. Improved Deposition of Large Scale Ordered Nanosphere Monolayers via Liquid Surface Self-Assembly. *Mater. Sci. Eng., B* **2009**, *165* (3), 186−189.

(32) Bennett, J. M.; Ashley, E. J. Infrared Reflectance and Emittance of Silver and Gold Evaporated in Ultrahigh Vacuum. *Appl. Opt.* **1965**, *4* (2), 221.

(33) Ginn, J.; Brener, I.; Peters, D.; Wendt, J.; Stevens, J.; Hines, P.; Basilio, L.; Warne, L.; Ihlefeld, J.; Clem, P.; Sinclair, M. Realizing Optical Magnetism from Dielectric Metamaterials. *Phys. Rev. Lett.*, **2012**, *108*.

(34) Zhao, Q.; Kang, L.; Du, B.; Zhao, H.; Xie, Q.; Huang, X.; Li, B.; Zhou, J.; Li, L. Experimental Demonstration of Isotropic Negative Permeability in a Three-Dimensional Dielectric Composite. *Phys. Rev. Lett.* **2008**, *101* (2), 027402.

(35) Decker, M.; Staude, I.; Falkner, M.; Dominguez, J.; Neshev, D. N.; Brener, I.; Pertsch, T.; Kivshar, Y. S. High-Efficiency Dielectric Huygens' Surfaces. *Adv. Opt. Mater.* **2015**, DOI: 10.1002/adom.201400584.